Supplementary information:

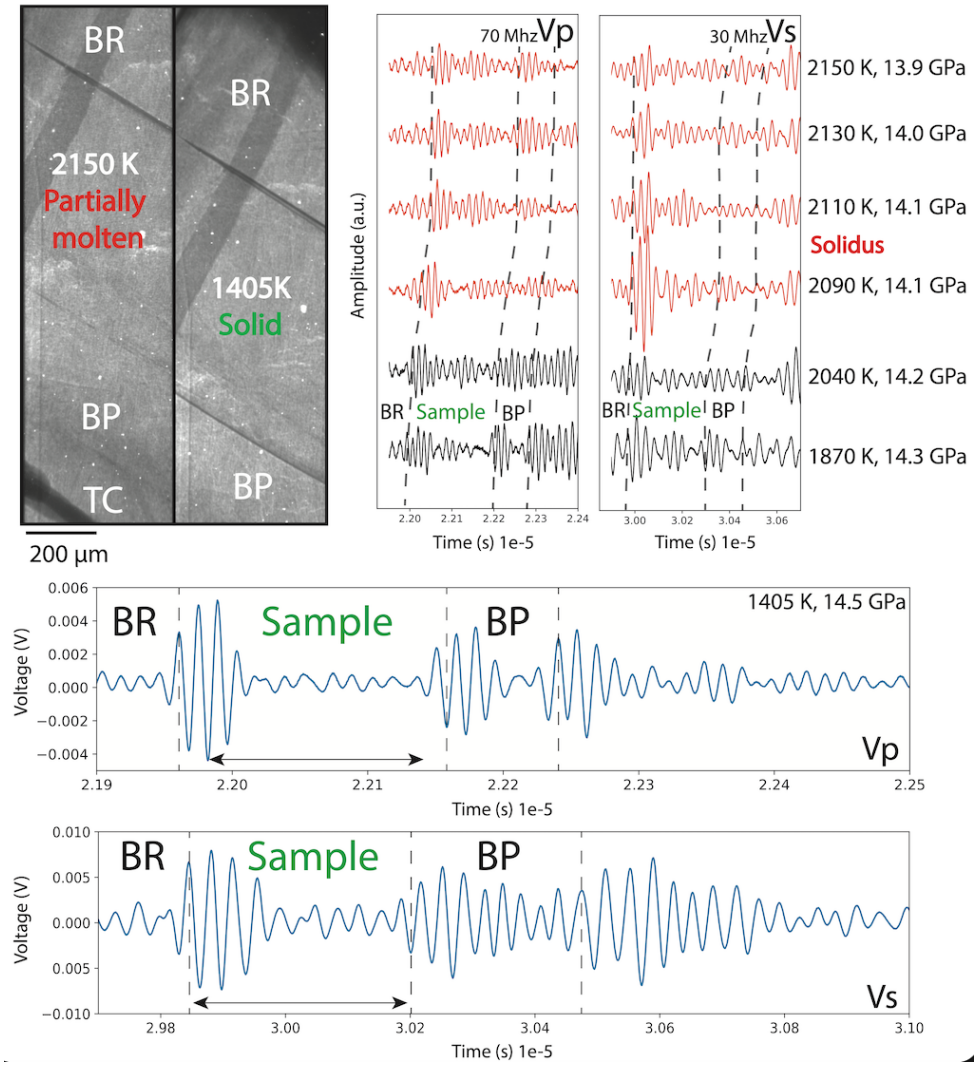

Fig S1. High-pressure ultrasonic measurements during melting experiments on a Martian mantle analogue at ~14 GPa. Left panel: X-ray radiography images of the sample assembly showing the buffer rod (BR), the sample, and the backing plate (BP) under fully solid conditions (1405 K) and at high temperature (2150 K, partially molten). The position of the thermocouple (TC) is indicated. Interfaces between BR, sample, and BP are defined by 2-µm-thick molybdenum foils. The change in sample geometry and image contrast with temperature is consistent with the onset of partial melting. Central panels: Time-domain ultrasonic waveforms for compressional (Vp, 70 MHz) and shear (Vs, 30 MHz) waves acquired during stepwise heating from subsolidus to supersolidus conditions (1870–2150 K,14.3 - 13.9 Gpa). The approximate position of the solidus is indicated. Bottom panels: Representative high-resolution Vp and Vs waveforms collected at 1405 K and 14.5 GPa, highlighting the arrival times from the buffer rod (BR), the sample, and the backing plate (BP), used to determine travel times and seismic velocities.

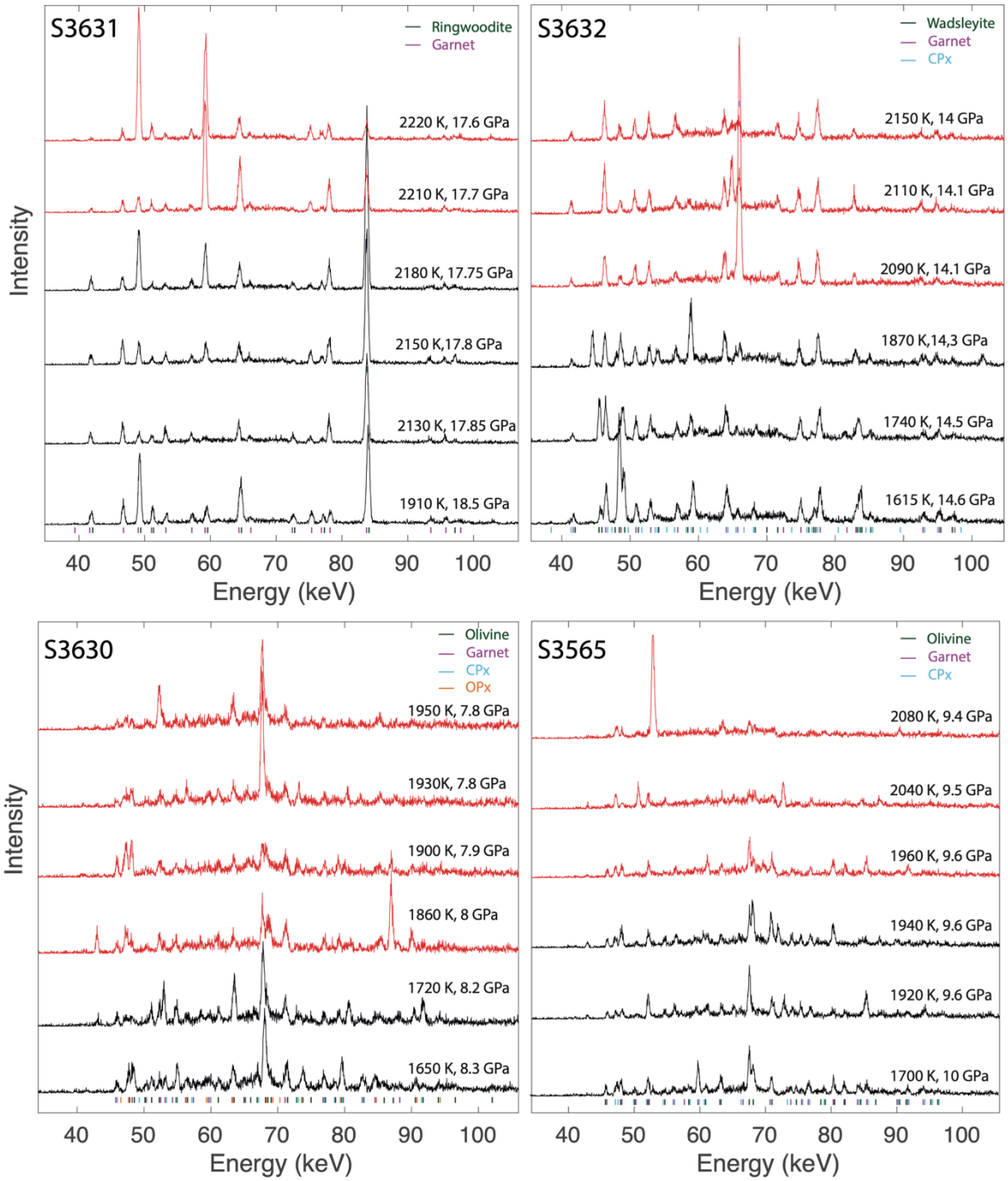

Fig S2. *In situ* energy-dispersive X-ray diffraction (ED-XRD) patterns for runs S3631, S3632, S3630 and S3565 at high pressure. Black spectra correspond to fully crystalline samples, with sharp Bragg reflections characteristic of garnet, ringwoodite/wadsleyite/olivine, and residual pyroxene. Red spectra correspond to the moment where progressive loss of crystallinity is observed, including peak broadening, quick reduced/increased intensities, and enhancement of diffuse backgrounds. These diffraction sequences provide direct *in situ* evidence of the onset of melting in Fe-rich Martian mantle analogues, allowing the solidus to be constrained with a precision of ±20–30 K and confirming melting relations inferred independently from ultrasonic Vp–Vs measurements.

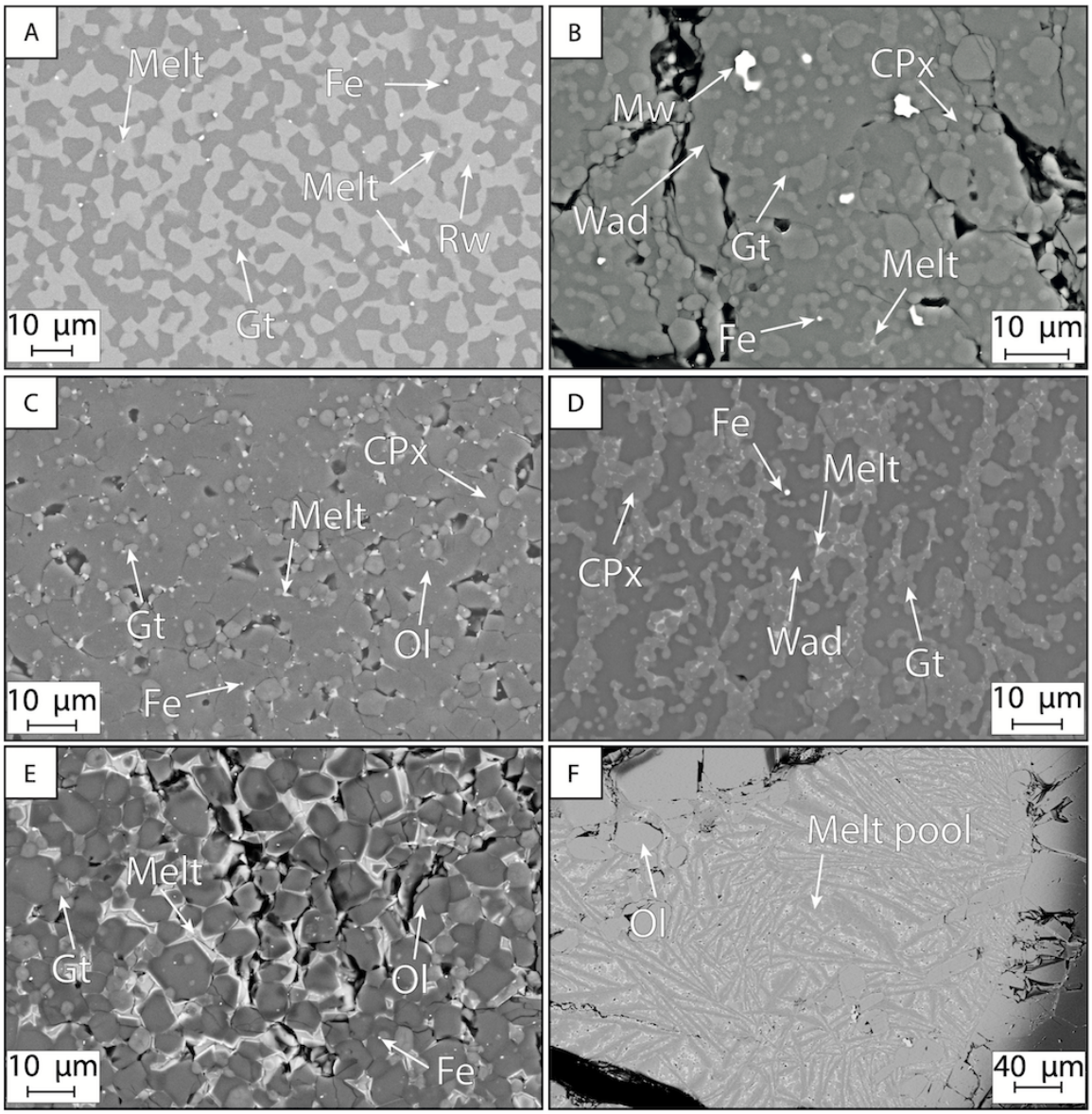

Fig S3. Backscattered electron (BSE) images illustrating melt fraction variations and phase distribution at different pressure-temperature conditions. Microstructural observations from BSE imaging reveal distinct textural and compositional changes associated with progressive melting: (A) S3631 and (B) S3632 (small colder region situated close to the buffer rod): Low-degree melting. Melt pockets are finely distributed along grain boundaries, suggesting incipient melting. (C) S3630 and S3632 (center of the sample): increasing melt fraction leads to the formation of interconnected melt networks, indicating enhanced connectivity and a more pervasive melting regime wich suggests conditions approaching the percolation threshold. (E) S3630 (hotspot) and (D) S3565: well-developed melt pathways, showing evidence of interconnected networks that facilitate melt migration. Formation of a large melt pools, displaying dendritic crystallization textures, suggesting rapid quenching from a high-temperature, largely molten state.

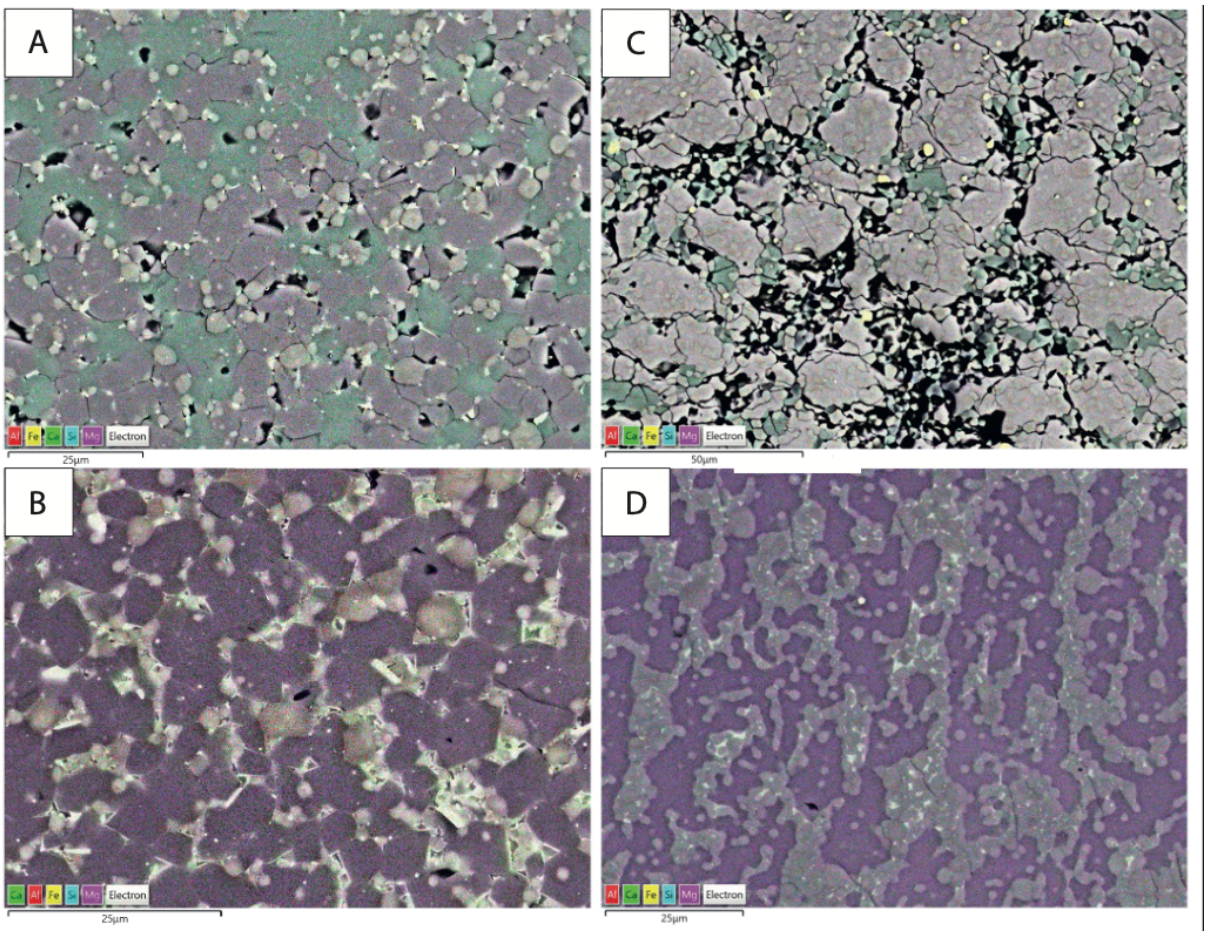

Fig S4. Scanning electron microscopy chemical maps. A) and B) Sample S3630; It shows two partially molten samples at low (A) and moderate (B) melt fractions. At solidus conditions, clinopyroxene (Cpx, green) is abundant between 8 and 10 GPa. Olivine appears in violet and garnet in orange/red. The distribution reveals that the melt is enriched in calcium and iron, consistent with partial melting of a source dominated by Cpx. (C) MA-14: Phase assemblage at higher pressure (14 GPa) under subsolidus conditions. At this stage, the amount of clinopyroxene decreases while garnet becomes more abundant, reflecting a shift in the equilibrium mineralogy. (D) Sample S3632 partially molten samples at moderate melt fractions below 15%. This scenario represents conditions close to the solidus, where residual phases dominate and the melt is minimal. Olivine appears in violet and garnet in red/grey. The melt between the grains is enriched in calcium and iron; it appears yellow/green. The distribution reveals that the melt is enriched in calcium and iron The different element used to generate the maps and their color are given at the bottom left corner of each map (the indication “electron” indicates the superposition with BSE microphotograph, which can help to see grain boundaries).

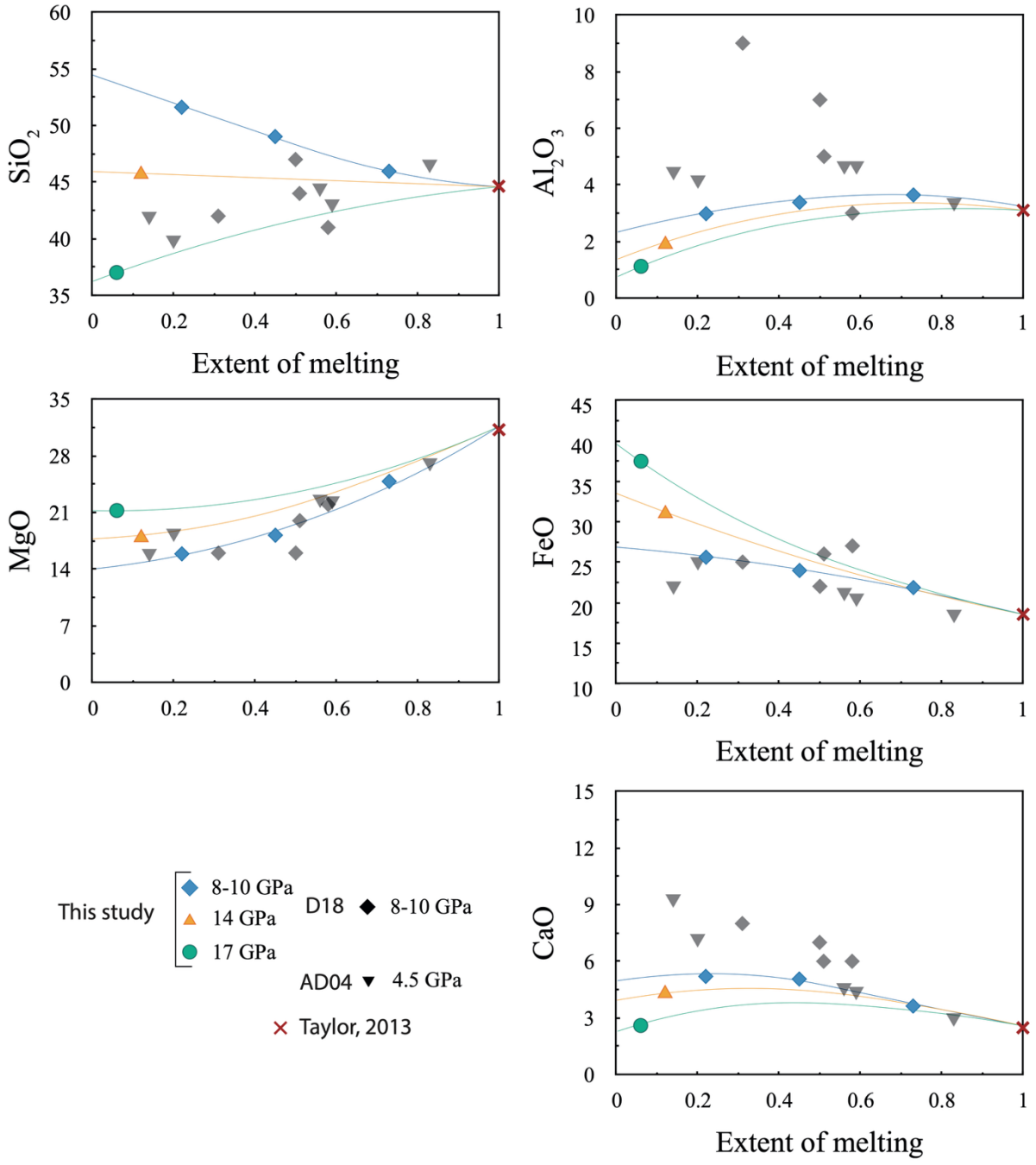

Fig S5. Variation diagrams showing oxide abundances of melt versus extent of melting (wt%). Averages of several electron microprobe analyses in the melt regions of our samples are plotted as colored symbols, for P between 8 and 17 GPa. One SD is <5% for each melt composition. The grey values correpond to chemistry of melt's literature [1,2] at various pressures and degrees of mantle melting.

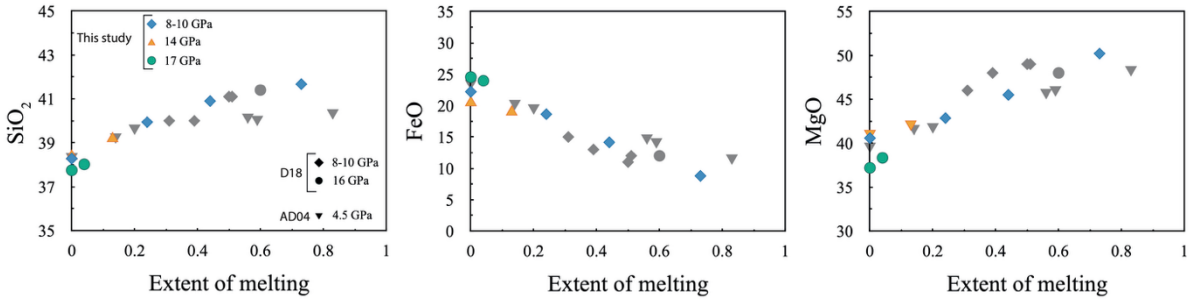

Fig S6. Variation diagrams showing oxide abundances of olivine and polymorphs versus extent of melting (wt%). Averages of several electron microprobe analyses in the melt regions of our samples are plotted as colored symbols, for P between 8 and 17 GPa. One SD is <5% for each melt composition. The grey values correpond to chemistry of melt's literature [1,2] at various pressures and degrees of mantle melting.

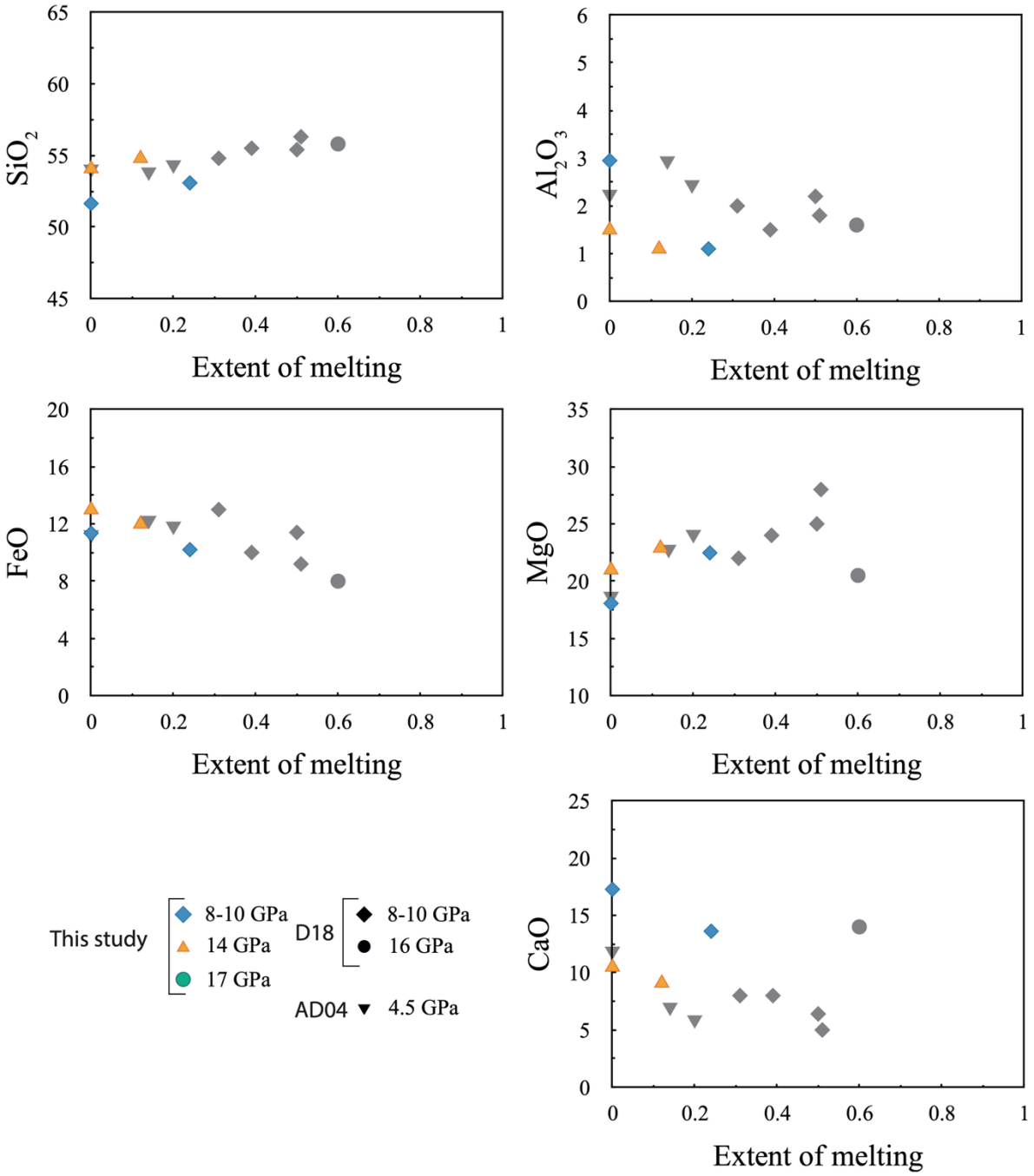

Fig S7. Variation diagrams showing oxide abundances of clinopyroxene versus extent of melting (wt%). Averages of several electron microprobe analyses in the melt regions of our samples are plotted as colored symbols, for P between 8 and 17 GPa. One SD is <5% for each melt composition. The grey values correpond to chemistry of melt's literature [1,2] at various pressures and degrees of mantle melting.

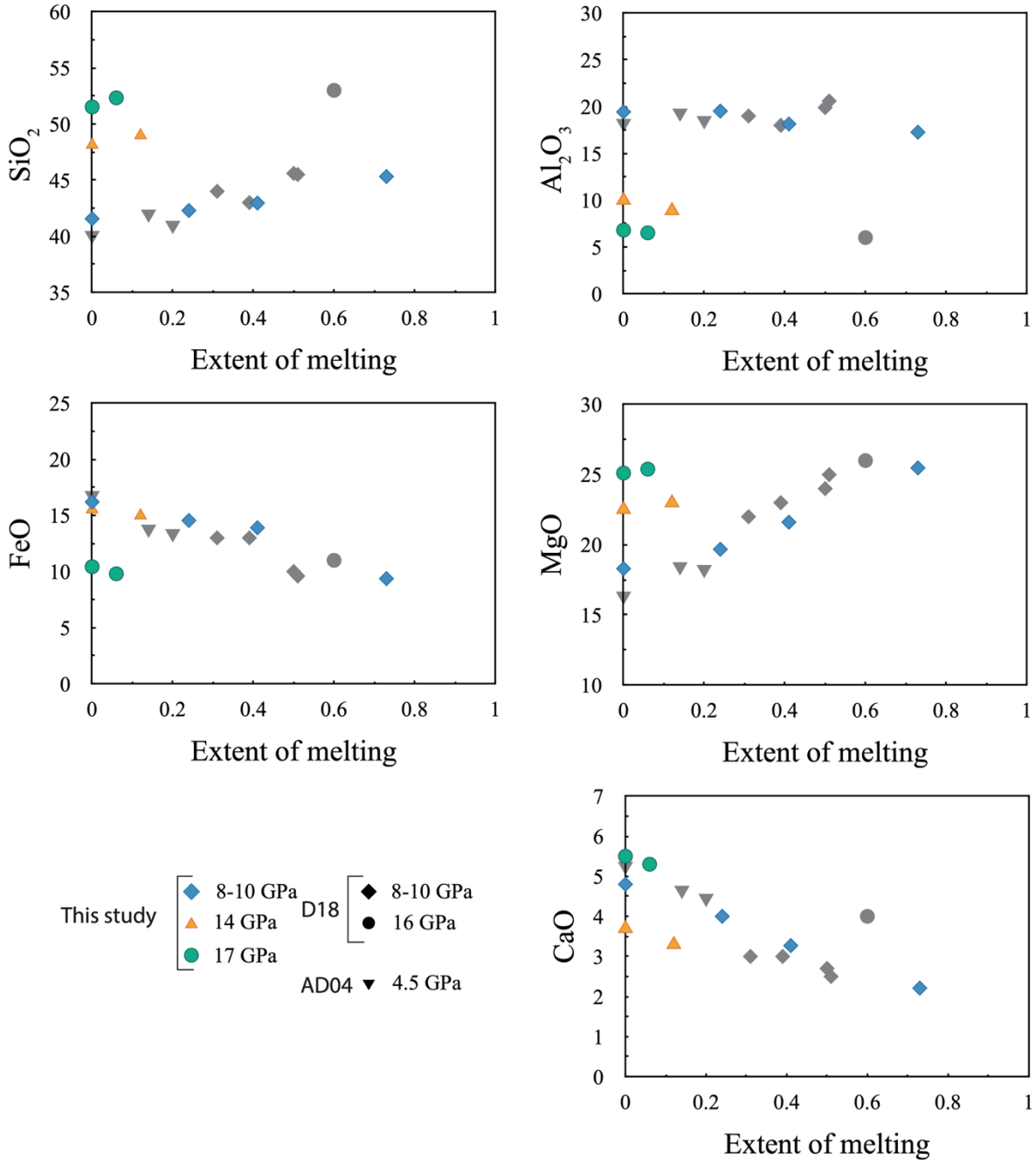

Fig S8. Variation diagrams showing oxide abundances of garnet versus extent of melting (wt%). Averages of several electron microprobe analyses in the melt regions of our samples are plotted as colored symbols, for P between 8 and 17 GPa. One SD is <5% for each melt composition. The grey values correpond to chemistry of melt's literature [1,2] at various pressures and degrees of mantle melting.

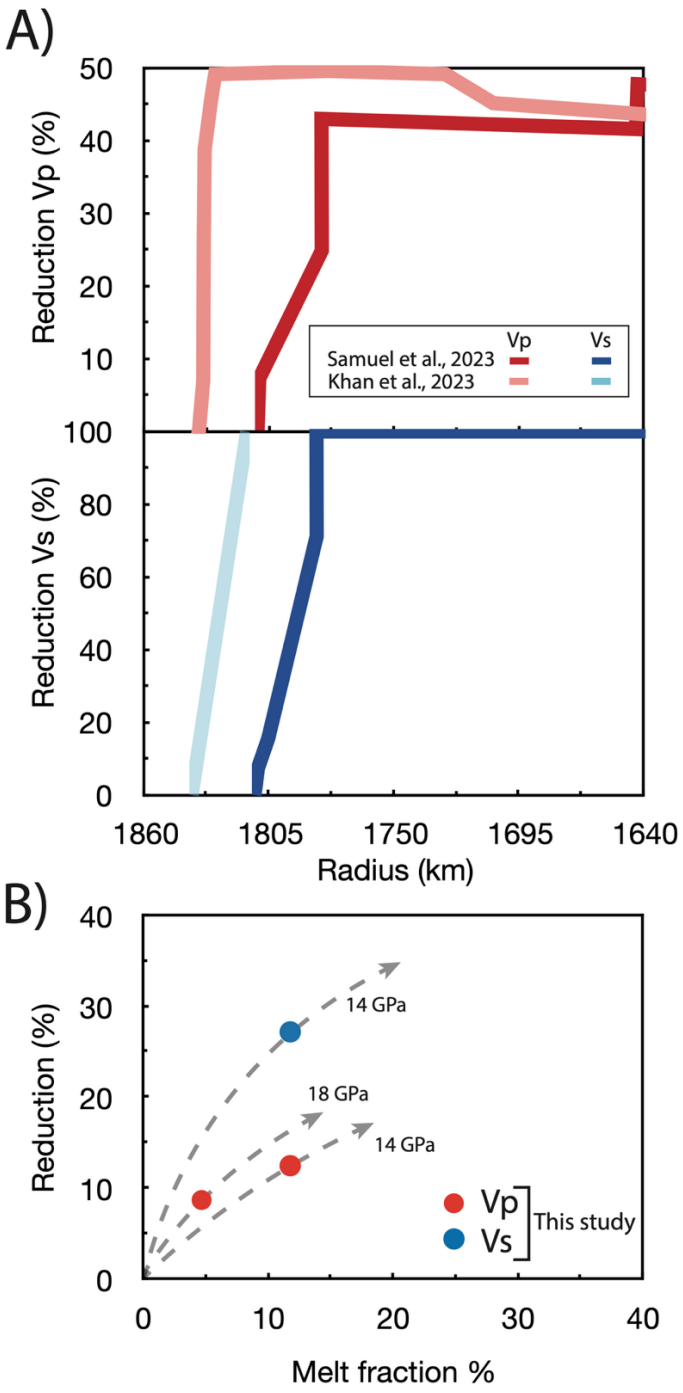

Fig S9. Seismic velocity reduction from InSight measured at the CMB compared to experimental reduction according to melt fraction. (A) and **(B)** compare the experimental results of this study with seismic models from [3,4], highlighting regions where the observed velocity reductions match the low-velocity zones predicted for Mars. The data suggest that even a small amount of melt significantly affects seismic velocities, potentially corresponding to partially molten layers in the deep mantle.

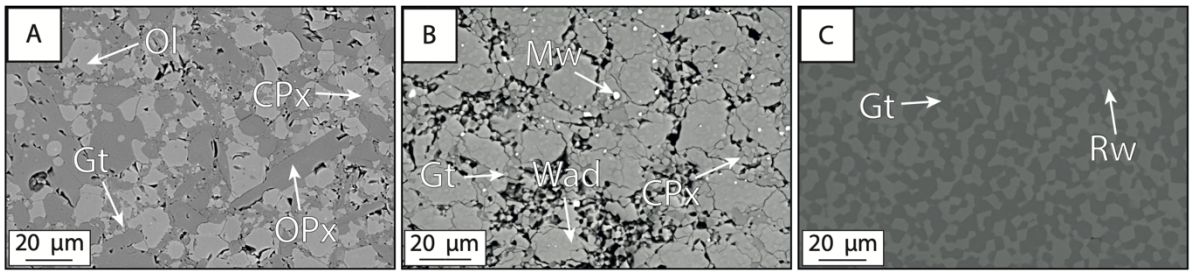

Fig. S10: **Backscattered electron images of sub-solidus mineralogical assemblages synthesized for ultrasonic experiments.** A) MA-5: The shallow-mantle experiment at 5 GPa results in a mixture of olivine (Ol), pyroxene (CPx + OPx), garnet (Gt). B) MA-14: The mid-mantle phase assemblage synthetized at 14 GPa contains Wadsleyite (Wad), clinopyroxene (CPx), garnet (Gt), magnesiowüstite (Mw) and the presence of metallic iron (Fe^0). C) MA-17: The deep mantle phase assemblage synthetized at 17 GPa contains ringwoodite (Rw) and garnet (Gt). The black areas are voids in the samples formed during sample polishing prior to SEM analyses and were not present during the high pressure and temperature experiments.

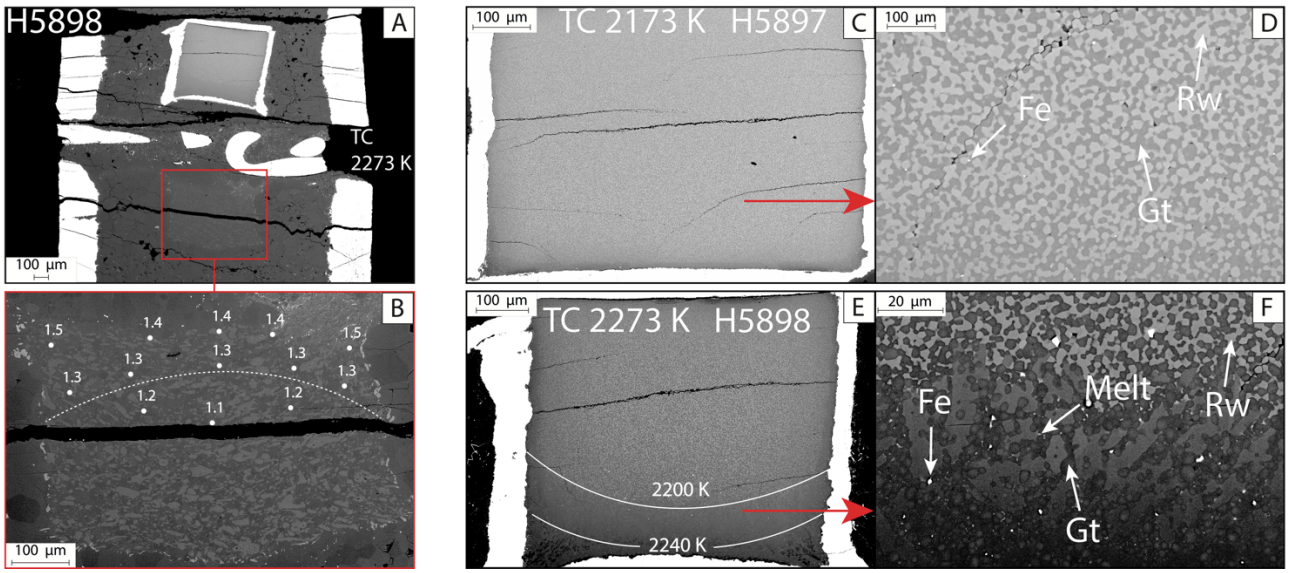

Fig. S11: Thermal gradients, redox conditions, and melt distribution in *ex situ* quench experiments made at BGI around 18 GPa. (A) BSE image of run H5898 showing the central portion of the BGI 10/4 assembly. The W–Re thermocouple (TC) was positioned at the center of the assembly and recorded 2273 K. A MgO–Al_2O_3 sample ("periclase marker") was placed on the opposite side of the TC to quantify thermal gradients across the assembly [5]. (B) Enlarged view of the periclase marker from (A). Numbers denote Al_2O_3 concentrations (mol%) measured in (Mg,Al)O. Because Al incorporation in periclase is temperature-dependent, these values define isotherms across the capsule. (C) BSE image of run H5897 quenched at a lower central temperature (2173 K). No silicate melt is observed, but exsolution of metallic Fe^0 occurs throughout the sample, reflecting the low oxygen fugacity imposed by the molybdenum capsule. (D) High-magnification image of H5897 showing grains of ringwoodite (Rw), garnet (Gt), and dispersed Fe^0 droplets. (E) BSE image of run H5898 (TC = 2273 K), displaying pronounced thermal gradients across the sample. Curved isotherms, inferred from Al_2O_3 zoning in the periclase marker, bracket the onset of melting around ~2200 ± 20 K. (F) Zoom of the hottest region in (E), showing interstitial silicate melt along grain boundaries coexisting with ringwoodite (Rw), garnet (Gt), and metallic Fe^0. The presence of melt at 18 GPa independently confirms the solidus determined from *in situ* ultrasonic and XRD measurements, while Fe^0 indicates redox conditions near or below the IW buffer.

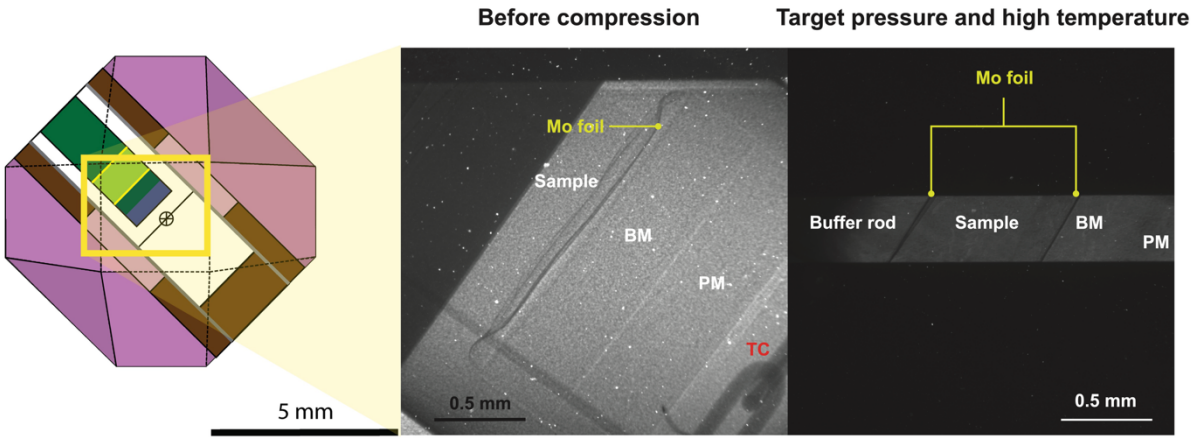

Fig. S12 Schematic diagram of the 10/5 high-pressure cell used in the present ultrasonic experiments. Buffer rod, Al2O3; sample, martian mantle analogue previously synthesised; pressure marker (gold and hBN with Mgo or NaCl); soft medium, MgO; pressure medium, (Mg,Co)O; insulator, LaCrO3. ⊗ denotes the thermocouple hot junction.

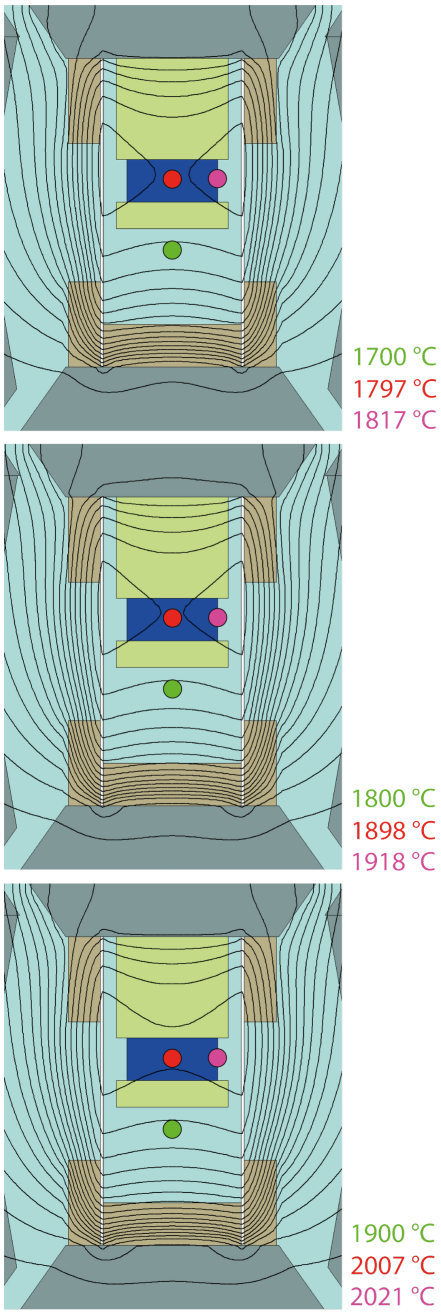

Fig. S13 Schematic thermal structure of the 10/5 multi-anvil high-pressure assembly used for ultrasonic measurements. Cross-sections show modelled temperature fields at nominal furnace setpoints of 1700 °C, 1800 °C and 1900 °C. Temperature distributions were calculated using the Cell Assembly software (Hernlund et al., 2006), highlighting the development of strong axial thermal gradients within the sample region. Isotherms are spaced by 100 °C. The experimental stack comprises, from the centre outward: Al_2O_3 buffer rods, a pre-synthesised Martian mantle analogue, pressure markers (MgO, Au and BN), a soft MgO medium, a (Mg,Co)O pressure medium, and a rhenium heater. The green circle marks the position of the thermocouple hot junction, whereas the red circles indicate calculated temperatures within the sample.

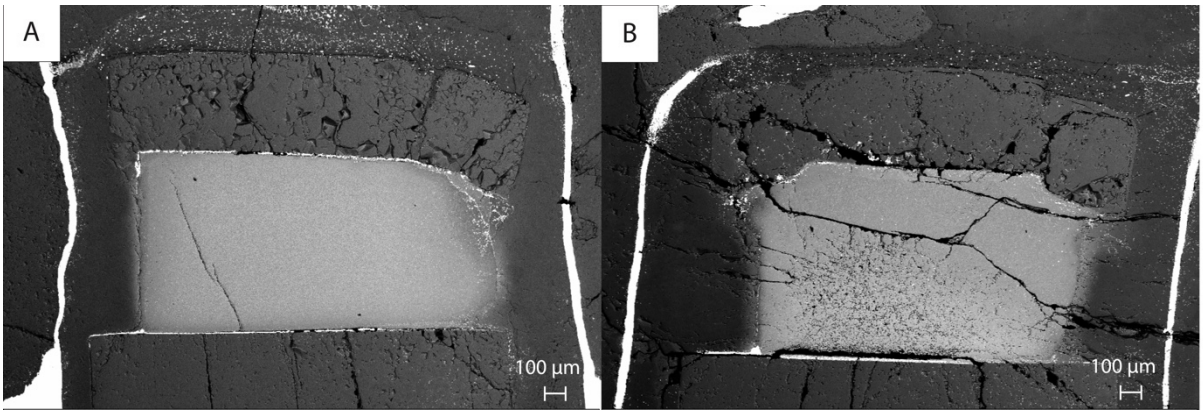

Fig S14. Backscattered electron (BSE) images of recovered samples from ultrasonic experiments. (a) Sample S3631; (b) Sample S3632. Both images show polished cross-sections of the central capsule region.

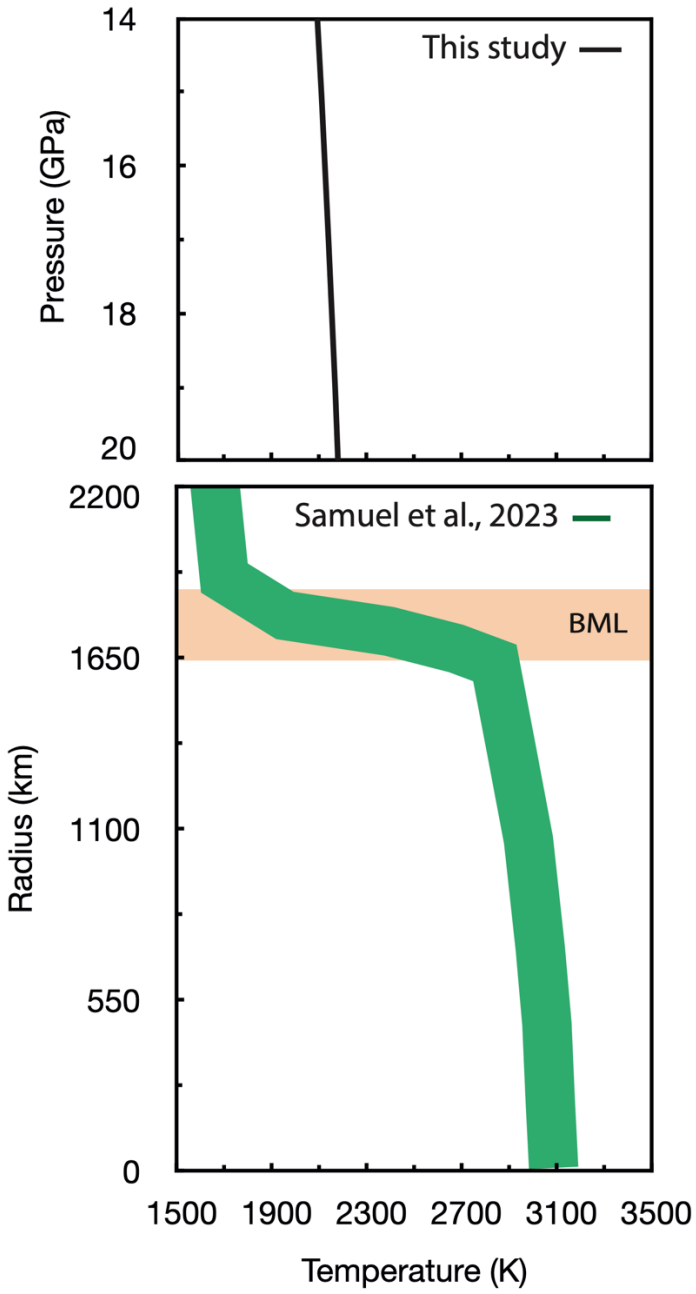

Fig S15. Temperature profile used to calculate the density of the $Fe_{0.5}$ liquid composition in the pressure range of 14–18 GPa. Top panel: The temperature profile adopted in this study (black line), plotted as a function of pressure. Bottom panel: Temperature profiles from recent interior models of Mars constrained by InSight seismic and geodetic data (green band), from [3], plotted as a function of planetary radius. These models suggest temperatures of approximately between 1900 and 2300 K at the base of the mantle, corresponding to the basal magma layer, which supports the profile adopted in this work.

Supplementary Note : Localized magma-ocean crystallization and volumetric constraints on basal magma ocean formation

To evaluate whether iron-rich melts produced during magma-ocean crystallization can plausibly account for the basal melt layer inferred at the Martian core–mantle boundary (CMB), we combine a first-order Fe–Mg partitioning model with simple geometric constraints on the volume of a basal magma layer. This approach is intended to test the plausibility of generating sufficiently Fe-rich melts prior to gravitational overturn, rather than to model the full thermo-chemical evolution of the Martian mantle.

1. Assumptions and initial conditions

The evolution of melt iron enrichment during crystallization was modelled assuming a localized magma-ocean domain crystallizing as a crystal-rich mush, such that newly formed solids remain partially coupled to the liquid. This regime is better approximated by equilibrium ("batch") crystallization than by perfect fractional (Rayleigh) separation.

The melt iron number is defined as:

(Eq. S1)

$$Fe\# = Fe / (Fe + Mg)$$

where Fe and Mg are molar proportions in the liquid.

The corresponding Fe/Mg ratio is:

(Eq. S2)

$$(Fe/Mg) = Fe\# / (1 - Fe\#)$$

We adopt an initial primitive Martian melt composition with:

(Eq. S3)

$$Fe\#^0 = 0.25$$

corresponding to an initial Fe/Mg ratio:

(Eq. S4)

$$(Fe/Mg)^0 = Fe\#^0/(1 - Fe\#^0)$$

The variable F denotes the fraction of melt remaining during crystallization, with F = 1 corresponding to the fully molten initial state.

2. Fe–Mg partitioning and batch crystallization model

Iron enrichment during crystallization is governed by Fe–Mg exchange between solids and melt, described by the partition coefficient:

(Eq. S5)

$$K_D^{Fe-Mg} = (Fe/Mg)_{solid}/(Fe/Mg)_{liquid}$$

Experimentally constrained values measured in this study span:

$$K_D^{Fe-Mg} = 0.20 - 0.35$$

To account for the presence of multiple crystallizing phases, we introduce effective bulk partition coefficients for Mg and Fe, denoted D_{Mg} and D_{Fe}, respectively, related by:

(Eq. S6)

$$D_{Fe} = K_D^{Fe-Mg} \times D_{Mg}$$

Effective bulk values of D_{Mg} in the range 1.2–2.5 were explored to represent plausible variations in crystallizing assemblages at deep mantle conditions. The explored range reflects plausible bulk partitioning behavior for Mg in deep-mantle crystallizing assemblages dominated by olivine/ringwoodite and majoritic garnet, consistent with experimental constraints on peridotitic systems at high pressure (e.g., [6,7]).

For equilibrium (batch) crystallization, the concentration of a component i in the liquid evolves as:

(Eq. S7)

$$C_{liq,i} = C_{0,i}/[F + (1 - F)D_i]$$

Applying Eq. (S7) to Fe and Mg and forming their ratio yields the evolution of the melt Fe/Mg ratio:

(Eq. S8)

$$\left(\frac{Fe}{Mg}\right)_{liq} = \left(\frac{Fe}{Mg}\right)_0 \frac{F + (1-F)D_{Mg}}{F + (1-F)D_{Fe}}, \quad \text{with } D_{Fe} = K_D^{Fe-Mg} D_{Mg}$$

The corresponding melt iron number is obtained by:

(Eq. S9)

$$Fe\#_{liq}(F) = (Fe/Mg)_{liq} / \left[1 + (Fe/Mg)_{liq}\right]$$

This formulation yields conservative enrichment trajectories relative to Rayleigh fractional crystallization and is therefore more appropriate for localized or mush-dominated magma-ocean settings.

3. Iron enrichment and gravitational instability

For experimentally constrained values of K_D^{Fe-Mg} and plausible bulk partition coefficients, the calculation shows that residual melts can progressively reach Fe# values comparable to those measured in our deep-mantle melting experiments (Fe# $\gtrsim$ 0.45–0.55). This calculation does not predict the timing of gravitational overturn directly, but instead constrains the compositional conditions under which residual melts may become neutrally to negatively buoyant at deep mantle pressures, once melt segregation and transport become dynamically feasible. However, it is important to note that the timing and dynamics of melt segregation and overturn will depend on mantle viscosity, melt connectivity, and thermal structure, which are beyond the scope of this first-order calculation.

4. Volumetric constraints from the basal magma layer

Independently, we estimated the fraction of the Martian mantle that must melt in order to generate a basal magma ocean (BMO) of the thickness inferred from geophysical models. We follow the geometric configuration proposed by [3,4], in which the basal melt layer is located immediately above the core–mantle boundary (CMB) and extends radially from 1650 km to 1830 km from the centre of Mars, corresponding to a thickness of ~180 km.

To compute the corresponding melt volume, Mars is approximated as a series of concentric spherical shells. We adopt a mean Martian radius of 3390 km and a core radius of ~1800 km, consistent with InSight-based interior models. To focus on the silicate mantle, we exclude an average crustal thickness of ~50 km, such that the outer radius of the mantle shell is taken as 3340 km.

The total volume of the silicate mantle, V_{mantle}, is therefore calculated as the volume of a spherical shell bounded by radii of 1800 km and 3340 km:

(Eq. S10)

$$V_{mantle} = \frac{4}{3}\pi(3340^3 - 1800^3)$$

The volume of the basal magma ocean, V_{BMO}, is computed using the same spherical shell formulation, bounded by radii of 1650 km and 1830 km:

(Eq. S11)

$$V_{BMO} = \frac{4}{3}\pi(1830^3 - 1650^3)$$

Using these values, the total silicate mantle volume is 1.316×10^{11} km³, while the basal magma ocean volume is 6.854×10^{9} km³. The inferred basal magma ocean therefore represents approximately 5 % of the Martian silicate mantle volume.

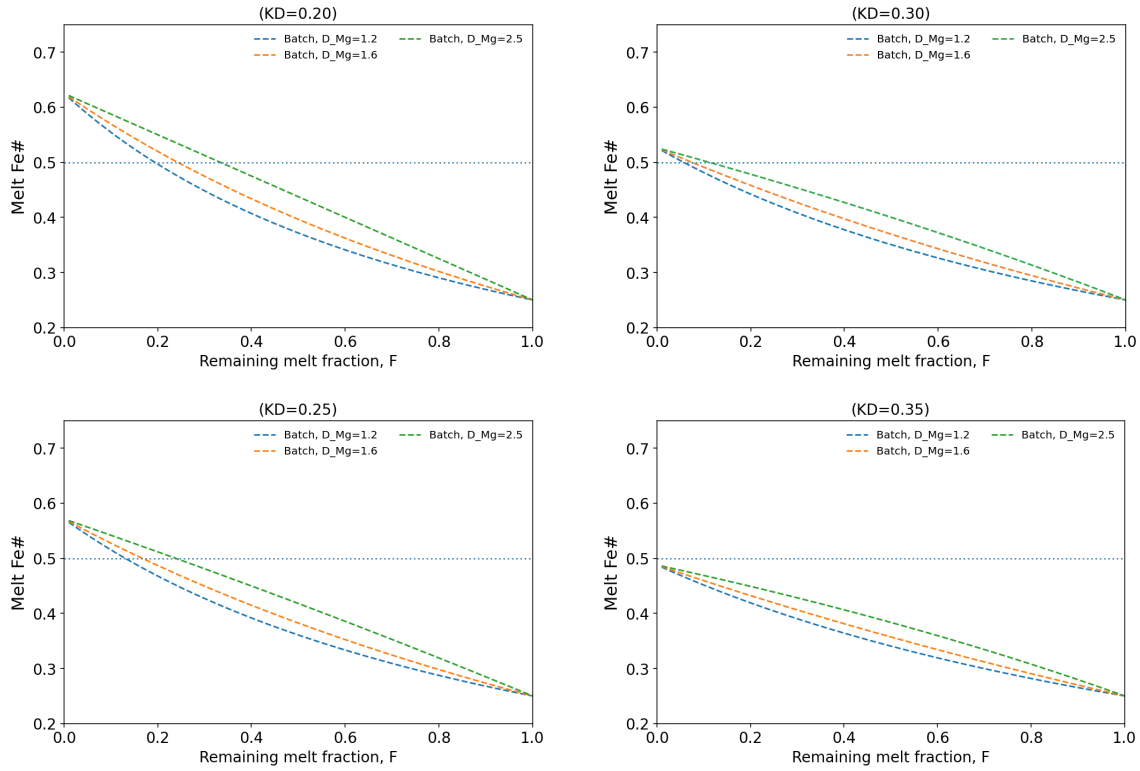

Figure S16: Iron enrichment of residual melts during crystallization of a localized magma ocean. Evolution of melt iron number (Fe# = Fe/(Fe+Mg)) as a function of the remaining melt fraction F during crystallization of a localized Martian magma-ocean reservoir. Dashed lines show equilibrium (batch) crystallization, representative of crystal-rich mush or localized magma-ocean domains where solids remain in chemical communication with the melt. Calculations are shown for different effective bulk Mg partition coefficients (D_{Mg} = 1.2,\ 1.6,\ 2.5), and for four values of the experimentally constrained Fe–Mg exchange coefficient (K_D^{Fe-Mg} = 0.35,\ 0.30,\ 0.25,\ 0.20; panel titles). The horizontal dotted line indicates Fe# = 0.50, corresponding to the iron-rich melt compositions measured in high-pressure melting experiments.

5. Implications

This simple geometric estimate provides an order-of-magnitude constraint on the amount of melt required to form a basal magma ocean of the thickness suggested by seismic observations. Because it assumes a fully molten basal layer of fixed thickness, this estimate represents an upper bound; variations in layer thickness or melt fraction would translate into uncertainties of only a few percent in the inferred mantle melt volume. Importantly, this fraction remains small relative to the total mantle volume, indicating that the formation of a volumetrically significant basal melt layer does not require extensive or long-lived global melting, but can instead result from melt segregation and accumulation during localized magma-ocean crystallization followed by gravitational overturn.

Taken together, the volumetric constraint (~5 % of the silicate mantle) and the experimentally determined Fe–Mg partitioning provide quantitative bounds on the conditions under which a basal magma ocean or basal melt layer may form in the Martian lowermost mantle. In equilibrium (batch) crystallization within partially molten, crystal-rich mush zones, the remaining melt fraction required to generate Fe-rich residual liquids decreases systematically with increasing Fe–Mg partitioning. For the experimentally constrained range of K_D^{Fe-Mg}, residual melts with Fe# ≥ 0.45–0.55 are produced once the remaining melt fraction falls below ~20 % for K_D^{Fe-Mg}= 0.20, below ~10 % for K_D^{Fe-Mg}= 0.25–0.30, and below ~5 % for K_D^{Fe-Mg}= 0.35 (Fig. S16). At deep mantle pressures, such Fe-rich melts are expected to be neutrally to negatively buoyant, promoting melt segregation, gravitational overturn, and accumulation at the core–mantle boundary. These values are consistent with the volumetric fraction of melt inferred from seismic observations for the basal melt layer, even if larger volumes of melt may transiently accumulate at the base of the mantle.

Over time, such deep melts are expected to partially crystallize and re-equilibrate with the overlying solid mantle, ultimately yielding residual melt volumes comparable to or lower than ~5 % and producing a diffusive zone of iron-rich solid material at the core–mantle boundary.

The combination of modest required melt volumes and enhanced melt density therefore provides a physically consistent pathway for the formation of a long-lived basal melt layer. This framework reconciles seismic evidence for low-velocity zones near the Martian CMB with experimental constraints on melt composition and density.

References

1. Duncan, M. S., Schmerr, N. C., Bertka, C. M. & Fei, Y. Extending the Solidus for a Model Iron-Rich Martian Mantle Composition to 25 GPa. *Geophys. Res. Lett.* 45, 10,211-10,220 (2018).
2. Agee, C. B. & Draper, D. S. Experimental constraints on the origin of Martian meteorites and the composition of the Martian mantle. *Earth Planet. Sci. Lett.* 224, 415–429 (2004).
3. Samuel, H. *et al.* Geophysical evidence for an enriched molten silicate layer above Mars's core. *Nature* 622, 712–717 (2023).
4. Khan, A. *et al.* Evidence for a liquid silicate layer atop the Martian core. *Nature* 622, 718–723 (2023).
5. Man, L. *et al.* Alumina solubility in periclase determined to lower mantle conditions and implications for ferropericlase inclusions in diamonds. *Geochim. Cosmochim. Acta* 375, 36–49 (2024).
6. Matsukage, K. N., Nagayo, Y., Whitaker, M. L., Takahashi, E. & Kawasaki, T. Melting of the Martian mantle from 1.0 to 4.5 GPa. *Journal of Mineralogical and Petrological Sciences* 108, 201–214 (2013).
7. Walter, M. J. Melting of garnet peridotite and the origin of komatiite and depleted lithosphere. *Journal of Petrology* 39, 29–60 (1998).